Cation-substitution-tuned oxygen electrocatalyst of spinel cobaltite MCo_2O_4 (M = Fe, Co, and Ni) hexagonal nanoplates for rechargeable Zn-air batteries

Peng Tan[1,3,†], Zhen Wu[2,3,†], Bin Chen[3,4], Haoran Xu[3], Weizi Cai[3], Shaowei Jin[5], Zongping Shao[6,7], Meng Ni[3,*]

[1]Department of Thermal Science and Energy Engineering, University of Science and Technology of China, Hefei 230026, China

[2]Shaanxi Key Laboratory of Energy Chemical Process Intensification, School of Chemical Engineering and Technology, Xi'an Jiaotong University, Xi'an 710049, China

[3]Department of Building and Real Estate, The Hong Kong Polytechnic University, Hung Hom, Kowloon, Hong Kong, China

[4]Institute of Deep Earth Sciences and Green Energy, Shenzhen University, Shenzhen 518060, China

[5]National Supercomputing Center in Shenzhen, Shenzhen 518055, China

[6]State Key Laboratory of Materials-Oriented Chemical Engineering, College of Chemical Engineering, Nanjing Tech University, No. 30 South Puzu Road, Nanjing 211816, China

[7]Department of Chemical Engineering, Curtin University, Perth, WA 6845, Australia

*Corresponding author. E-mail: meng.ni@polyu.edu.hk (Meng Ni)

[†]These authors contributed equally to this work.

Abstract: The spinel cobalt oxide (Co_3O_4) nanoplate exposed with hexagonal {111} facets is demonstrated to be a highly active catalyst, while the effect of cation substitution on the oxygen electrocatalysis is still unclear. Herein, the electrocatalytic activity of cation-substituted spinel cobaltite MCo_2O_4 (M = Fe, Co, and Ni) nanoplates with the {111} facets is investigated systematically by experiments and theoretical calculations. For both oxygen reduction and evolution reactions, Ni-substituted Co_3O_4 hexagonal nanoplates show the best activity. It is mainly attributed to the increased surface energy per unit area and the enhanced oxygen species absorption ability, which are also evidenced by density functional theory calculations. Moreover, the three kinds of MCo_2O_4 nanoplates are applied in Zn-air batteries

and the corresponding electrochemical performance is tested. Among the three batteries, $NiCo_2O_4$ hexagonal nanoplates also enable the highest peak power density of 110.3 mW cm^{-2} and the most stable discharge-charge voltage profiles for 50 cycles, indicating that $NiCo_2O_4$ nanoplates are the promising catalyst for further Zn-air battery applications. Besides, this work illustrates that the substitution of Co by Ni or Fe can remarkably change the electronic structural states, thus tuning the electrochemical properties of the hexagonal Co_3O_4 nanoplates.

Keywords: Catalysis; Computational analysis; Electrochemistry; Spinel cobaltite; Cation substitution

1. Introduction

With the rapid demand of energy in electronic devices, the electrochemical energy storage systems have attracted great research attention, especially metal-air batteries (e.g., Li-air and Zn-air batteries).[1–5] Based on the mechanism of oxygen reduction reaction (ORR), metal-air batteries can provide significantly higher capacities (e.g., 3862 mAh g^{-1} for Li-air batteries) than conventional Li-ion batteries, which can enable much higher duration for electronic devices.[6,7] Thus, effective catalysts with high activity toward oxygen electrocatalysis are the key to the implementation of this technology.[8] Although Pt exhibits the excellent ORR activity, the high price and the limited stability have hindered its wide application.[9] In addition, for rechargeable metal-air batteries, high activity toward the oxygen evolution reaction (OER) is essential,[10] which is unfortunately absent in Pt.[11,12] Therefore, developing newly effective catalysts with high electrochemical performance toward both ORR and OER is crucial for energy conversion systems.[13–15]

To date, considerable interests have been put on transition metals and their oxides.[16–19] Among them, the spinel cobalt oxide (Co_3O_4) is the most studied one owing to its high activity, high capacitance, and low cost.[20–25] For example, Chen et al. reported Co_3O_4 nanodisks as a bifunctional catalyst in Zn-air batteries, which exhibited highly efficient electrochemical performance and superior rechargeability, and no voltage drops were

observed over 60 pulse cycles.[26] Yan et al. synthesized Co_3O_4 nanoarrays on nickel foam substrates with different morphologies and found that the rectangular nanosheets exhibited superior electrocatalytic performance compared with nanowires and hexagonal nanosheets, leading to the higher capacity and better cycling stability of Li-O_2 batteries.[27] Wang et al. fabricated single crystalline Co_3O_4 nanocrystals exposed with different crystal planes. Combining experimental and theoretical investigations, they showed that the essential factor to promote the OER in Li-O_2 batteries is the surface crystal planes, which is in the order of {100} < {110} < {112} < {111}.[28] However, the relatively low electrical conductivity affects electron transport, leading to lower electrochemical performance than expectations.[29]

To overcome this issue, modifications on Co_3O_4 have been reported, such as combining with other materials to form composites[30–32] and partially replacing Co to form ternary spinel cobaltites.[33–38] As Co_3O_4 has an intrinsic spinel structure with Co^{2+} and Co^{3+} occupying the tetrahedral and octahedral interstices, the partial substitution of Co by the transition metals can provide ion diffusion channels and change the electrical conductivity. Liu et al. fabricated spinel MCo_2O_4 with the porous nanorod structure in which Co was substituted by Mn, Fe, Ni, and Zn. Attributed to the highest Co^{3+} ratio on the $FeCo_2O_4$ surface, oxygen could be easily adsorbed onto the active sites and reduced. Consequently, the $FeCo_2O_4$ cathode enabled the lowest overpotential, the highest capacity, and the best cycling performance of Li-O_2 batteries.[39] Jun et al. investigated the effect of cation substitution (Mn, Ni, and Cu) on the pseudocapacitive performance of spinel cobaltite mesoporous nanowires, and found that $MnCo_2O_4$ could achieve the highest specific capacitance due to the enhanced charge transfer and ion diffusion.[40] Although Co_3O_4 nanoplate exposed with {111} facets has been demonstrated to be an effective catalyst, the effect of cation substitution on the oxygen electrocatalysis of spinel cobaltite with {111} facets remains unclear.

Herein, we systematically investigated the electrocatalytic activity of spinel cobaltite MCo_2O_4 (M = Fe, Co, and Ni) nanoplates with the hexagonal morphology by experiments and

theoretical calculations in this work. The spinel cobaltite MCo_2O_4 (M = Fe, Co, and Ni) nanoplates with {111} facets were first synthesized and characterized. Then, the electrochemical performance toward the ORR and OER processes was investigated in the alkaline solution to discuss the effect of cation M substitution on the oxygen electrocatalytic activity. Further, Zn-air batteries with MCo_2O_4 nanoplates as catalysts were tested, including the discharge and charge polarization, power density, and cycling stability. This work serves to reveal the mechanism of cation substitution, and provides strategies for developing high active catalysts for energy conversion systems.

2. Method

2.1 Material synthesis and characterization

The spinel cobaltite MCo_2O_4 (M = Fe, Co, and Ni) nanoplates were synthesized using a modified method for fabricating Co_3O_4 nanoplates.[41,42] Briefly, 1 mmol of metal nitrates (Fe, Co, and Ni) and 2 mmol of cobalt nitrate were dissolved in 30 mL of distilled water. Then, the NaOH solution was slowly dropped with stirring until the pH value reached 10. The mixture was vigorously stirred for 10 min at room temperature and transferred to Teflon-lined stainless steel autoclaves. After hydrothermal reaction at 180 °C for 4 h, the samples were washed with distilled water and dried at 60 °C overnight. The obtained precursors were calcined in air at 300 ^{o}C for 3 hours with a temperature ramp of 1 ^{o}C min^{-1}.

The compositions of the synthesized samples were analyzed by X-ray diffraction (XRD, Rigaku Smartlab) with a Cu-Kα source at 40 keV. The morphologies were observed by a transmission electron microscope (TEM, JEOL 2100F) under the voltage of 200 kV. To determine the geometrical properties, nitrogen adsorption-desorption isotherms were measured by ASAP 2020, and the Brunaure-Emmert-Teller and Barrett-Joyner-Halenda methods were used to determine the specific surface area and pore structure, respectively.

To evaluate the electrochemical properties of MCo_2O_4 nanoplates in alkaline media, a three-electrode cell with 0.1 M KOH aqueous solution was applied, and the measurements

were conducted using a Solartron potentiostat by rotating disc electrode (RDE) voltammetry. To prepare the working electrode, the catalyst ink with MCo_2O_4 nanoplates was first made according to our previous work,[42] which was then dripped onto the polished glassy carbon electrode and dried completely, and the catalyst loading was estimated to be 0.2 mg cm^{-2}. The counter and reference electrodes were a platinum wire and a Hg/HgO electrode, respectively. The ORR activity was measured in the oxygen-saturated electrolyte. Linear sweep voltammetry (LSV) was conducted within the potential from 0.2 to −0.7 V (vs. Hg/HgO) using a scan rate of 5 mV s^{-1}, and the rotation speed changed from 400 to 2500 rpm. The Koutecky-Levich equation was used to determine the number of electrons transferred (n):[43]

$$j^{-1} = j_k^{-1} + j_d^{-1} \quad (1)$$

$$j_d = 0.2nFD_{O_2}^{2/3}v^{-1/6}C_{O_2}\omega^{1/2} \quad (2)$$

where j, j_k, and j_d are the measured, kinetic, and diffusion-limiting current densities, respectively. F is the Faraday constant (96485 C mol^{-1}), D_{O_2} and C_{O_2} are the diffusion coefficient (1.86×10^{-5} cm^2 s^{-1}) and the bulk concentration (1.21×10^{-6} mol cm^{-3}) of oxygen in 0.1 M KOH, respectively. v is the kinematic viscosity of 0.1 M KOH (1.01×10^{-2} cm^2 s^{-1}), and ω is the angular velocity (rpm). The ORR stability test was performed by recording the current density at a constant potential of −0.465 V (vs. Hg/HgO). The OER activity was measured within the potential from 0.2 to 0.9 V (vs. Hg/HgO) using a scan rate of 5 mV s^{-1} at a rotation speed of 1600 rpm. The OER stability test was performed through recording the potential a constant current density of 10 mA cm^{-2}. To clearly present the results, all potentials were calibrated to a reversible hydrogen electrode (RHE) scale.[44]

2.2 Theoretical calculations

The DFT calculations using the Vienna Ab initio Simulation Package (VASP) were performed to theoretically investigate the effect of substitution Fe or Ni on the oxygen electrocatalytic activity of Co_3O_4 oxide with spinel structure.[45,46] During the calculations of

total energy (TOTEN), the generalized-gradient approximation (GGA)-PBE functional was adopted to estimate the exchange-correlation energy (an important component of the TOTEN),[47] and the self-consistent field (SCF) iteration method was used to solve the Kohn-Sham (K-S) equation.[48] During the iteration process, the Pulay mixture density was chosen to address the electron relaxation in the SCF approximation.[49] The spin polarization was considered for DFT calculations because of the transition metals Ni, Fe, and Co with magnetism involved in the MCo_2O_4 (M=Co, Ni, and Fe) spinel oxides. The geometry optimization of the initial MCo_2O_4 crystal structures was performed to get the most stable structures prior to the calculations of TOTEN and electronic properties. The computational modeling of the MCo_2O_4 crystal structure exposed with the {111} facets is described in Supporting Information (SI) and the corresponding models are demonstrated in Fig. S1 according to the experimental SEM morphology.

A plane wave basis set was used with the cutoff energy of 320 eV, and Monkhorst-Pack k-point was set as 3 × 3 × 3 for the crystal structures of MCo_2O_4 bulk. For the corresponding {111} facets, 500 eV and a 6 × 6 × 1 Monkhorst-Pack k point mesh were chosen for the cutoff energy and the Brillouin zone integration, respectively. The tolerances of energy and force were set as 10^{-5} eV and 0.02 eV·Å^{-1}, respectively. On the basis of the previous reports, the GGA+*U* (Hubbard *U* model) approach with the U_{eff} values of 3.52,[50] 4.0,[51] and 4.0 eV [52] was applied for a better description of the 3d electrons of the element Co, Ni, and Fe in our calculations, respectively. The valence-electron configurations for the Co, Ni, Fe, and O were chosen as $3d^7 4s^2$, $3d^8 4s^2$, $3d^6 4s^2$, and $2s^2 2p^4$, respectively.

2.3 Battery assembly and test

A catalyst ink was made by mixing 50 wt% of active carbon (Vulcan XC 72), 25 wt% of active material (MCo_2O_4 nanoplates), and 25 wt% of polytetrafluoroethylene (PTFE) binder with ethanol to form a homogenous mixture. The air electrode was prepared by spraying the ink onto a gas diffusion layer (carbon paper, Toray 060), and the catalyst loading was 2 mg

cm^{-2}. A Zn-air battery was composed of a Zn foil as the metal electrode, the as-prepared air electrode, and 6 M KOH with 0.2 M zinc acetate as the electrolyte.[25] The charge and discharge polarization curves of the battery were measured at a current step of 1 mA s^{-1}. The cycling stability was tested at 5 mA cm^{-2} with a fixed time interval of 20 min for each cycle.

3. Results and discussion

3.1 Phase and crystal structure characterization

Figure 1a to 1c show the XRD patterns of MCo_2O_4 (M = Fe, Co, and Ni) nanoplates, which reveal the peaks of (111), (220), (311), (222), (400), (422), (511), and (440) corresponding to $FeCo_2O_4$ (JCPDS #71-0816), Co_3O_4 (JCPDS #42-1467), and $NiCo_2O_4$ (JCPDS #73-1702), respectively.[39] The TEM images are shown in Fig. 2 to present the morphologies and structures of MCo_2O_4 nanoplates. From the low-magnification images in Fig. 2a, 2d, and 2g, hexagonal-shaped nanoplates with diameters of ~150 nm and thicknesses of ~20 nm are observed, demonstrating that after the substitution of other metal ions, the hexagonal morphology is preserved. In addition, the nanoplates have a porous structure, which is attributed to the release of water molecules and volume shrinkage during the calcination process.[53] From Fig. 2b, 2e, and 2h, it is interesting to find that with the substitution element changes from Fe to Ni, the size of nanoparticles that form the hexagonal plates decreases, resulting in smaller pore size. To confirm this observation, nitrogen isothermal adsorption-desorption measurements were conducted, and the results are shown in Fig. 3. All of the samples exhibit combined I/IV isotherms with distinct hysteresis loops, indicating the coexistence of micropores and mesopores. The specific surface areas of $FeCo_2O_4$, Co_3O_4, and $NiCo_2O_4$ are calculated to be 76.0, 81.5, and 85.9 m^2 g^{-1}, respectively. From Fig. 3 insets, the pore size distribution of $FeCo_2O_4$, Co_3O_4, and $NiCo_2O_4$ mainly range from 2−50, 2−15, and 2−10 nm, and the corresponding pore volumes are calculated to be 0.42, 0.35, and 0.30 cm^3 g^{-1}, respectively, which are consistent with the TEM observations. The high-resolution TEM image displayed in Fig. 2c shows the interplaner spacings of 0.243 and

187 0.285 nm, which correspond to the (311) and (220) planes of $FeCo_2O_4$. The interplaner
188 spacing shown in Fig. 2f is indexed to the (220) crystal planes of the Co_3O_4 crystal. The
189 interplanar spacing of 0.245 nm shown in Fig. 2i agrees well with the (311) plane of $NiCo_2O_4$.
190 Thus, porous MCo_2O_4 nanoplates with hexagonal shapes were successfully synthesized.

191 To characterize the valence states of MCo_2O_4 nanoplates, XPS measurements were
192 carried out, and the results are shown in Fig. 4. Fig. 4a and 4b show the XPS spectra of Fe 2p
193 and Ni 2p, respectively. In Fig. 4a, two peaks are observed at 711.1 and 724.3 eV, which are
194 ascribed to the spin-orbit peaks of the Fe $2p_{3/2}$ and Fe $2p_{1/2}$, respectively. In addition, a
195 satellite peak at 715.8 eV is characterized to Fe^{2+}.[39] These results indicate that Fe^{2+} is the main
196 species on the surface of $FeCo_2O_4$. Fig. 4b shows the Ni 2p XPS spectrum, in which the two
197 observed peaks of Ni $2p_{3/2}$ and Ni $2p_{1/2}$ at 853.8 and 871.9 eV are ascribed to Ni^{2+}, and at
198 855.6 and 873.8 eV are ascribed to Ni^{3+}, indicating the mixed valence of Ni in $NiCo_2O_4$. Fig.
199 4c shows the Co 2p spectra of MCo_2O_4 (M = Fe, Co, and Ni). These two peaks at around
200 780.0 and 795.5 eV are ascribed to Co^{3+}, and other two peaks at around 781.1 and 796.4 eV
201 are ascribed to Co^{2+}, demonstrating the coexistence of Co^{2+} and Co^{3+} on the surface.

202 *3.2 Electrochemical performance*

203 The ORR activity of MCo_2O_4 nanoplates with the hexagonal morphology was tested in
204 the 0.1 M KOH electrolyte. Fig. 5a-c present the LSV curves of $FeCo_2O_4$, Co_3O_4, and
205 $NiCo_2O_4$ nanoplates at different rotating rates, and the insets present the corresponding
206 Koutecky-Levich plots. For three samples, a linear increase of the current density is observed
207 with an increase of the rotating rate, and the average number of electrons transferred is
208 calculated to be ~4, indicating a four-electron ORR process. To compare the effects of
209 element substitution on the ORR activity, the LSV curves at the rotating speed of 1600 rpm
210 are compared, as shown in Fig. 5d, and the corresponding Tafel plots are presented in Fig. 5e.
211 The Co_3O_4 nanoplate exhibits an onset potential of 0.82 V and a limiting current density of
212 4.87 mA cm^{-2} (0.2 V vs. RHE), and the Tafel slope is 114.3 mV dec^{-1}. After the substitution

of Fe, the onset potential decreases to 0.65 V, the limiting current density decrease to 4.72 mA cm^{-2}, and the Tafel slope becomes 119.7 mV dec^{-1}. In comparison, the substitution of Ni improves the onset potential to 0.83 V, and the limiting current density and Tafel slope become 4.91 mA cm^{-2} and 100.8 mV dec^{-1}, respectively. Hence, the $FeCo_2O_4$ nanoplate presents the reduced ORR activity while the $NiCo_2O_4$ nanoplate exhibits improved ORR activity. Moreover, the stability of MCo_2O_4 nanoplates during the ORR process was measured by recording the current density at 0.2 V for 10 h. As shown in Fig. 5f, $NiCo_2O_4$ nanoplate preserves 93.3% of its initial current density, higher than Co_3O_4 (83.5%) and $FeCo_2O_4$ (80.0%). Thus, $NiCo_2O_4$ demonstrates the best ORR performance among these three spinel cobaltite MCo_2O_4.

Through the density functional theory (DFT) calculations, it was found that the superior ORR performance of $NiCo_2O_4$ is mainly attributed to the increased surface energy per unit area (E_{surf}) and the enhanced oxygen species absorption ability caused by the Ni substitution. The calculation equation of E_{surf} is expressed in Eq. S3 (Supporting Information).[28] Table 1 lists the calculated surface energies of MCo_2O_4 oxides. The value of pure Co_3O_4 oxides is calculated to be 2.71 J m^{-2}, which agrees well with the previously reported surface energy per unit area of Co_3O_4 (2.31 J m^{-2}).[54] The small difference may be ascribed to the consideration of GGA+*U* approach used in our calculations. The Hubbard *U* model is usually considered to more accurately predict the electronic properties of transition metal oxides involving d and f orbital electrons.[55,56] When the element Ni is substituted for Co, the surface energy of $NiCo_2O_4$ oxide increases to 2.93 J m^{-2}, indicating an enlarged density of low-coordinated atoms with high reactivity on the surface.[57] The high-energy surface is also regarded to have a great contribution to facilitating the oxygen ion transfer between the surface and the interior.[58,59] Consequently, the Ni-substituted Co_3O_4 oxide exposed with higher surface energy demonstrates better catalytic activity than the pristine surface with lower surface energy. In contrast, the substitution of Fe for Co reduces the spinel Co_3O_4 surface energy per

unit area to 1.60 J m^{-2}. Therefore, the substitution of Ni facilitates the catalytic activity of spinel Co_3O_4 hexagonal nanoplates, while the Fe substitution has a negative effect on the catalytic activity, in accordance with our experimental results. In addition, the prediction on the cohesive energy and occupation energy (Table S1) was also found that the Ni substitution enhances the activity while the Fe substitution stabilizes the Co_3O_4 oxide, leading to different ORR performance of MCo_2O_4.

On the other hand, the O_2 molecule adsorption on the facet of hexagonal $NiCo_2O_4$ nanoplates is the most energetically favorable among the three kinds of MCo_2O_4 nanoplates. Fig. 6 shows the O_2 adsorption pathways on the MCo_2O_4 hexagonal facets and the corresponding adsorption energy, which visualize the O_2 adsorption and dissociation steps. The corresponding O_2 adsorption energy of the $NiCo_2O_4$ nanoplates is calculated to be -2.381 eV $f.u.^{-1}$, lower than those of Co_3O_4 (-0.798 eV $f.u.^{-1}$) and $FeCo_2O_4$ (-0.550 eV $f.u.^{-1}$). In addition, the $NiCo_2O_4$ nanoplates have the best catalysis activity on the O_2 molecule dissociation into $2O^*$ atoms and the adsorption of the O^* atoms on the {111} facet, which can be confirmed by the lowest energy (-2.880 eV $f.u.^{-1}$) for the $NiCo_2O_4$ hexagonal facet bonding with $2O^*$ atoms. In contrast, the O_2 adsorption, dissociation, and the O^* adsorption on the Co_3O_4 nanoplates are slightly reduced after the Fe substitution. The adsorption energy for both O_2 molecule and O^* atom is increased to -0.550 and -0.725 eV $f.u.^{-1}$, respectively. The increase in the adsorption energy (negative value) shows the weakened interactions between the surface and the adsorbates. The adsorption configurations of O_2 and O^* atoms on the $NiCo_2O_4$ hexagonal facet are also demonstrated in Fig. 6. The initial length of the O–O bond is 1.505 Å, but slightly elongates to 1.518 Å after the stable adsorption on the $NiCo_2O_4$ nanoplates. After the O_2 dissociation into $2O^*$ atoms, the relaxed O–O bond length is greatly enlarged into 3.093 Å, which is two times as long as the original one. Thus, the $NiCo_2O_4$ can firmly absorb O_2 molecule and successfully dissociate O_2 into $2O^*$ atoms. Fig. 7 shows the partial DOS (PDOS) of the adsorbate O^* atoms on the MCo_2O_4 nanoplates. Here, the Fermi

level (E_F) is set as zero and used as a reference for energy. It can be confirmed in Fig. 7 that the dissociative O^* atoms are stable in the Co–Ni bridge and Ni–Ni bridge sites with the bond lengths of 1.740 Å for Co–O1, 1.771 Å for Ni1–O1, 1.815 Å for Ni1–O2, and 1.990 Å for Ni2–O2.

As seen clearly from Fig. 7b, the stronger bonding interaction between Ni/Co and O atoms are confirmed by DOS results. The significant overlaps of almost all the PDOS peaks between Ni1/Ni2 3d and O1/O2 2p orbitals and between Co 3d and O1 2p orbitals appear in the energy region of about -7.5 eV ~ E_F. The DOS peak overlaps indicate strong hybridizations between Ni/Co 3d and O 2p orbital electrons in the O^* atoms adsorption system of the $NiCo_2O_4$, which contribute to the Ni–O and Co–O bonding with the corresponding lengths of 1.771~1.990 Å and 1.740 Å. Thus, the substitution of Ni causes the smaller Co^{3+}–O bonding lengths (from 1.865~2.021 Å to 1.771~1.990 Å), generating stronger bonding interaction. Accordingly, the amounts of charge transfer of Ni (substituting for Co) and O increase from 1.22~1.26 e to 1.60~1.71 e and from 0.85~1.01 e to 1.09 e, respectively (Table S2). Although the elongated Co^{2+}–O length from 1.727 to 1.740 Å indicates the reduced Co^{2+}–O bonding effect after the addition of Ni, the ORR catalytic activity of Ni-doped Co_3O_4 nanoplates is still regarded to be better than that of the pristine surface. That is mainly because the Co^{3+} is the main active sites in ORR for the MCo_2O_4 spinel structure.[39,60] In comparison, the Fe–O bonding effect was found to be weak in the $FeCo_2O_4$ nanoplates, which can be confirmed by the small PDOS overlap between Fe 3d and O 2p orbitals and the accordingly elongated Fe–O bonding lengths shown in Fig. 7c, as well as the decreased charge transfer between Fe and O listed in Table S2. It has been reported that the O_2 adsorption process plays a crucial role in the initial stage and thus affects the overall ORR catalytic performance.[61] Therefore, the enhanced oxygen species absorption ability is also viewed to be one of the reasons why Ni-substituted Co_3O_4 spinel with hexagonal morphology has superior ORR performance.

In addition to the ORR performance, the OER performance of MCo_2O_4 nanoplates was also evaluated, and results are shown in Fig. S2. As the LSV results shown in Figs. S2a and S2b, the Co_3O_4 nanoplate achieves the current density of 10 mA cm^{-2} at 1.638 V (vs. RHE) and exhibits a Tafel slope of 70.3 mV dec^{-1}. For the $FeCo_2O_4$ nanoplate, the potential at 10 mA cm^{-2} reduces to 1.620 V, and the Tafel slope decreases to 61.5 mV dec^{-1}. Thus, the substitution of Fe into Co_3O_4 improves the OER activity. For the $NiCo_2O_4$ nanoplate, the potential at 10 mA cm^{-2} and the Tafel slope further decrease to 1.571 V and 52.0 mV dec^{-1}, respectively, demonstrating the enhanced activity. The OER stability of these three kinds of MCo_2O_4 nanoplates was measured by recording the potential at 10 mA cm^{-2} for 10 h. As shown in Fig. S2c, the potential of $NiCo_2O_4$ nanoplates increases from 1.571 V to 1.579 V, with an increase of 8 mV. Similarly, $FeCo_2O_4$ nanoplates exhibit an increased potential of ~5 mV. However, for Co_3O_4 nanoplates, the potential increases from 1.638 V to 1.705 V, showing a remarkable potential change of 67 mV. The results illustrate that the substitution of Co by Fe or Ni can improve the OER performance MCo_2O_4 nanoplates, and $NiCo_2O_4$ nanoplates exhibit the best OER performance.

3.3 Application in Zn-air batteries

Previous research has demonstrated that Co_3O_4 nanoplates can be effective catalysts in rechargeable Zn-air batteries.[26,42] From the electrochemical performance of MCo_2O_4 hexagonal nanoplates with {111} facet in the alkaline solution, different ORR and OER activity are exhibited. To illustrate the practical application, MCo_2O_4 hexagonal nanoplates were used as the catalysts in home-made Zn-air batteries, and the performance is shown in Fig. 8. The discharge polarization curve of the battery with $NiCo_2O_4$ exhibited the highest voltages, followed by that with Co_3O_4, while the battery with $FeCo_2O_4$ shows the lowest discharge voltages. Consequently, the peak power density of the battery with $NiCo_2O_4$ researches 110.3 mW cm^{-2}, while those of the batteries with Co_3O_4 and $FeCo_2O_4$ are 102.0 and 97.2 mW cm^{-2}, respectively. For the charge process, as illustrated by the polarization curves in Fig. S3, the

battery with $NiCo_2O_4$ nanoplates delivers the lowest voltages, which researches 2.50 V when the current density increases to 83 mA cm^{-2}. For the batteries with Co_3O_4 and $FeCo_2O_4$, the charge voltages are similar, and the one with $FeCo_2O_4$ nanoplates exhibits little lower voltages, consistent with the electrochemical performance demonstrated in the alkaline solution.

The electrochemical stability of MCo_2O_4 nanoplates in rechargeable Zn-air batteries was further investigated by a pulse discharge-charge test. To avoid the corrosion of carbon support caused by the high potential [62] and make a fair comparison of MCo_2O_4 nanoplates, a relatively small current density of 5 mA cm^{-2} was applied. As shown in Fig. 9a, the initial discharge and charge voltages of the battery with $FeCo_2O_4$ are 1.203 and 1.996 V, respectively, with a voltage gap of 0.793 V. While after 50 cycles, the discharge and charge voltages become 1.108 and 2.026 V, and the voltage gap increases to 0.918 V. Similar results can be observed in the battery with Co_3O_4 nanoplates, from which the voltage gap increases from 0.840 to 0.949 V after 50 cycles (Fig. 9b). For the battery with $NiCo_2O_4$ nanoplates, the initial voltage gap is 0.814 V, and only increases to 0.879 V at the 50^{th} cycle, with an increase of 65 mV (Fig. 9c). Thus, $NiCo_2O_4$ nanoplates demonstrate the best discharge and charge performance, as well as the cycling stability, indicating the promising applications in rechargeable Zn-air batteries.

4. Conclusions

In summary, spinel cobaltite MCo_2O_4 (M = Fe, Co, and Ni) hexagonal nanoplates exposed with the {111} facets were investigated systematically by experimental and theoretical analyses. In experiments, $NiCo_2O_4$ nanoplates exhibited the highest onset potential of 0.83 V, the largest limiting current density of 4.91 mA cm^{-2}, and the lowest Tafel slope of 100.8 mV dec^{-1} for the oxygen reduction reaction among these three samples, in contrast to the $FeCo_2O_4$ nanoplates. Thus, the catalytic activity rank is Ni > Co > Fe for the cation substitution. The DFT calculations reveal that Ni substituting for Co helps to increase the

surface energy from 2.71 to 2.93 J m^{-2} and contributes to enhancing oxygen adsorption ability. The stronger bonding interaction between surface and adsorbate in $NiCo_2O_4$ nanoplates accounts for the better oxygen electrocatalytic activity, which is consistent with the experimental results. In addition, the oxygen evolution reaction performance of MCo_2O_4 nanoplates was examined, among which $NiCo_2O_4$ nanoplates also showed the best activity. Furthermore, the electrochemical performance of three kinds of MCo_2O_4 nanoplates was tested in Zn-air batteries. The $NiCo_2O_4$, Co_3O_4, and $FeCo_2O_4$ nanoplates enabled the peak power density of 110.3, 102.0, and 97.2 mW cm^{-2}, respectively, and the battery with $NiCo_2O_4$ nanoplates showed the best charge performance. After operating for 50 discharge-charge cycles, the voltage gap of the battery with $NiCo_2O_4$ nanoplates increased only 65 mV, demonstrating the best stability among these three samples. Thus, the results illustrate that the substitution of Co by transition metals (Ni and Fe) in spinel Co_3O_4 can remarkably change the electronic structural states and tune the electrochemical properties. Among them, $NiCo_2O_4$ hexagonal nanoplates exhibit the best ORR/OER activity and stability, which can be a promising catalyst for rechargeable Zn-air batteries and other energy conversion systems.

Supporting Information

Supporting Information to this article can be found online or from the authors.

Acknowledgements

P. Tan thanks the funding support from CAS Pioneer Hundred Talents Program and USTC Tang Scholar. Z. Wu thanks the funding support from the National Natural Science Foundation of China (21736008) and Hong Kong Scholar Program (XJ2017023). M. Ni thanks the funding support from The Hong Kong Polytechnic University (G-YBJN and G-YW2D), a fund from RISUD (1-ZVEA), and a grant (Project Number: PolyU 152214/17E) from Research Grant Council, University Grants Committee, Hong Kong SAR.

References

1. B. Chen, H. Xu, H. Zhang, P. Tan, W. Cai, M. Ni, *Appl. Energy*, **200**, 260–272 (2017).

2. H. Xu, B. Chen, P. Tan, H. Zhang, J. Yuan, J. Liu, M. Ni, *Energy*, **140**, 979–987 (2017).

3. Y. Li and H. Dai, *Chem. Soc. Rev.*, **43**, 5257–5275 (2014).

4. Z.-L. Wang, D. Xu, J.-J. Xu, and X.-B. Zhang, *Chem. Soc. Rev.*, **43**, 7746–7786 (2014).

5. M. Winter and R. J. Brodd, *Chem. Rev.*, **104**, 4245–4270 (2004).

6. M. A. Rahman, X. Wang, and C. Wen, *J. Electrochem. Soc.* , **160**, A1759–A1771 (2013).

7. J. Christensen, P. Albertus, R.S. Sanchez-Carrera, T. Lohmann, B. Kozinsky, R. Liedtke, J. Ahmed, A. Kojic, *J. Electrochem. Soc.*, **159**, R1 (2012).

8. D. Chen, C. Chen, Z. M. Baiyee, Z. Shao, and F. Ciucci, *Chem. Rev.*, **115**, 9869–9921 (2015).

9. P. Tan, M. Liu, Z. Shao, and M. Ni, *Adv. Energy Mater.*, **7**, 1602674 (2017).

10. P. Tan, H.R. Jiang, X.B. Zhu, L. An, C.Y. Jung, M.C. Wu, L. Shi, W. Shyy, T.S. Zhao, *Appl. Energy*, **204**, 780–806 (2017).

11. C. Tang, H.-F. Wang, X. Chen, B.-Q. Li, T.-Z. Hou, B. Zhang, Q. Zhang, M.-M. Titirici, F. Wei, *Adv. Mater.*, **28**, 6845–6851 (2016).

12. X. Liu, M. Park, M.G. Kim, S. Gupta, X. Wang, G. Wu, J. Cho, *Nano Energy*, **20**, 315–325 (2016).

13. D. U. Lee, P. Xu, Z.P. Cano, A.G. Kashkooli, M.G. Park, Z. Chen, *J. Mater. Chem. A*, **4**, 7107–7134 (2016).

14. P. Tan, B. Chen, H. Xu, H. Zhang, W. Cai, M. Ni, M. Liu, Z. Shao, *Energy Environ. Sci.*, **10**, 2056–2080 (2017).

15. P. Tan, B. Chen, H. Xu, H. Zhang, W. Cai, M. Chen, M. Ni, *J. Electrochem. Soc.*, **166**, A616–A622 (2019).

16. N.-T. Suen, S.-F. Hung, Q. Quan, N. Zhang, Y.-J. Xu, H.M. Chen, *Chem. Soc. Rev.*, **46**, 337–365 (2017).

17. Z.-F. Huang, J. Wang, Y. Peng, C.-Y. Jung, A. Fisher, X. Wang, *Adv. Energy Mater.*, **7**, 1700544 (2017).

18. P. Tan, B. Chen, H. Xu, W. Cai, M. Liu, Z. Shao, M. Ni, *J. Electrochem. Soc.*, **165**, A2119–A2126 (2018).

19. M. Xiong and D. G. Ivey, *J. Electrochem. Soc.*, **164**, A1012–A1021 (2017).

20. Q. Dong, N. Kumada, Y. Yonesaki, T. Takei, and N. Kinomura, *Mater. Res. Bull.*, **46**, 1156–1162 (2011).

21. Y. Sun, J. Liu, J. Song, S. Huang, N. Yang, J. Zhang, Y. Sun, Y. Zhu, *ChemCatChem*, **8**, 540–545 (2016).

22. W. Gou, X. Zhou, J. Li, and Y. Ma, *Mater. Lett.*, **180**, 207–211 (2016).

23. S. K. Singh, V. M. Dhavale, and S. Kurungot, *ACS Appl. Mater. Interfaces*, **7**, 21138–21149 (2015).

24. Q. Yang, Z. Lu, X. Sun, and J. Liu, *Sci. Rep.*, **3**, 3537 (2013).

25. P. Tan, B. Chen, H. Xu, W. Cai, W. He, M. Liu, Z. Shao, M. Ni, *Small*, **14**, 1800225 (2018).

26. D. U. Lee, J. Scott, H.W. Park, S. Abureden, J.Y. Choi, Z. Chen, *Electrochem. commun.*, **43**, 109–112 (2014).

27. M. He, P. Zhang, S. Xu, and X. Yan, *ACS Appl. Mater. Interfaces*, **8**, 23713–23720 (2016).

28. D. Su, S. Dou, and G. Wang, *Sci. Rep.*, **4**, 5767 (2014).

29. J. Zhang, F. Liu, J. P. Cheng, and X. B. Zhang, *ACS Appl. Mater. Interfaces*, **7**, 17630–17640 (2015).

30. N. Xu, J. Qiao, X. Zhang, C. Ma, S. Jian, Y. Liu, P. Pei, *Appl. Energy*, **175**, 495–504 (2016).

31. G. Du, X. Liu, Y. Zong, T.S.A. Hor, A. Yu, Z. Liu, *Nanoscale*, **5**, 4657–4661 (2013).

32. J.-H. Zhong, A.-L. Wang, G.-R. Li, J.-W. Wang, Y.-N. Ou, Y.-X. Tong, *J. Mater. Chem.*, **22**, 5656 (2012).

33. Y. Liu, L.-J. Cao, C.-W. Cao, M. Wang, K.-L. Leung, S.-S. Zeng, T.F. Hung, C.Y. Chung,

421 Z.-G. Lu, *Chem. Commun.*, **50**, 14635–14638 (2014).
422 34. H. S. Jadhav, R. S. Kalubarme, C.-N. Park, J. Kim, and C.-J. Park, *Nanoscale*, **6**, 10071–6
423 (2014).
424 35. G. Liu, L. Zhang, S. Wang, L.-X. Ding, and H. Wang, *J. Mater. Chem. A*, **5**, 14530–14536
425 (2017).
426 36. T. Y. Ma, Y. Zheng, S. Dai, M. Jaroniec, and S. Z. Qiao, *J. Mater. Chem. A*, **2**, 8676–8682
427 (2014).
428 37. C. Wei, Z. Feng, G.G. Scherer, J. Barber, Y. Shao-Horn, Z.J. Xu, *Adv. Mater.*, **29**, 1–8
429 (2017).
430 38. W. Sun, Y. Wang, H. Wu, Z. Wang, D. Rooney, K. Sun, *Chem. Commun.* (2017).
431 39. S. G. Mohamed, Y.-Q. Tsai, C.-J. Chen, Y.-T. Tsai, T.-F. Hung, W.-S. Chang, R.-S. Liu,
432 *ACS Appl. Mater. Interfaces*, **7**, 12038–12046 (2015).
433 40. S. Liu, D. Ni, H.-F. Li, K.N. Hui, C.-Y. Ouyang, S.C. Jun, *J. Mater. Chem. A*, **6**, 10674–
434 10685 (2018).
435 41. S. Zhang, X. Sun, Z. Zheng, and L. Zhang, *Catal. Commun.*, **113**, 19–22 (2018).
436 42. P. Tan, B. Chen, H. Xu, W. Cai, W. He, M. Ni, *Energy*, **166**, 1241–1248 (2019).
437 43. L. Zeng, T. S. Zhao, and L. An, *J. Mater. Chem. A*, **3**, 1410–1416 (2015).
438 44. F. Meng, H. Zhong, D. Bao, J. Yan, and X. Zhang, *J. Am. Chem. Soc.*, **138**, 10226–10231
439 (2016).
440 45. G. Kresse and J. Hafner, *Phys. Rev. B*, **47**, 558–561 (1993).
441 46. G. Kresse and J. Furthmüller, *Comput. Mater. Sci.*, **6**, 15–50 (1996).
442 47. J. P. J. Perdew, K. Burke, and M. Ernzerhof, *Phys. Rev. Lett.*, **77**, 3865–3868 (1996).
443 48. W. Kohn and L. J. Sham, *Phys. Rev.*, **140**, A1133--A1138 (1965).
444 49. G. P. Francis and M. C. Payne, *J. Phys. Condens. Matter*, **2**, 4395 (1990).
445 50. M. Bajdich, M. García-Mota, A. Vojvodic, J. K. Nørskov, and A. T. Bell, *J. Am. Chem.*
446 *Soc.*, **135**, 13521–13530 (2013).

51. V. N. Antonov, B. N. Harmon, and A. N. Yaresko, *Phys. Rev. B*, **67**, 024417 (2003).

52. A. Jain, G. Hautier, S.P. Ong, C.J. Moore, C.C. Fischer, K.A. Persson, G. Ceder, *Phys. Rev. B*, **84**, 045115 (2011).

53. Z. Zhu, J. Ping, X. Huang, J. Hu, Q. Chen, X. Ji, C.E. Banks, *J. Mater. Sci.*, **47**, 503–507 (2012).

54. D. Su, S. Dou, and G. Wang, *Sci. Rep.*, **4**, 5767 (2015).

55. V. I. Anisimov, in *Spectroscopy of Mott Insulators and Correlated Metals*, p. 106–116, Springer Berlin Heidelberg (1995).

56. S. L. Dudarev, G. A. Botton, S. Y. Savrasov, C. J. Humphreys, and A. P. Sutton, *Phys. Rev. B*, **57**, 1505–1509 (1998).

57. N. P. Lebedeva, M. T. M. Koper, J. M. Feliu, and R. A. van Santen, *J. Phys. Chem. B*, **106**, 12938–12947 (2002).

58. D. Zhang, M. Wen, P. Zhang, J. Zhu, G. Li, H. Li, *Langmuir*, **28**, 4543–4547 (2012).

59. J. S. Chen, H. Liu, S. Z. Qiao, and X. W. (David) Lou, *J. Mater. Chem.*, **21**, 5687–5692 (2011).

60. M. De Koninck, S.-C. Poirier, and B. Marsan, *J. Electrochem. Soc.* , **153**, A2103–A2110 (2006).

61. Y. Ji, M. Yang, H. Dong, L. Wang, T. Hou, Y. Li, *J. Mater. Chem. A*, **5**, 1734–1741 (2017).

62. S. Suren and S. Kheawhom, *J. Electrochem. Soc.*, **163**, A846–A850 (2016).

Table and Figure Captions

Table 1 The relaxed surface areas and surface energies per unit cell of spinel MCo_2O_4 {111} facets.

Fig. 1. XRD patterns of MCo_2O_4 nanoplates. (a) $FeCo_2O_4$, (b) Co_3O_4, and (c) $NiCo_2O_4$.

Fig. 2. TEM images of MCo_2O_4 nanoplates with different magnifications. (a-c) $FeCo_2O_4$, (d-f) Co_3O_4, and (g-i) $NiCo_2O_4$.

Fig. 3. Nitrogen adsorption-desorption isotherms of MCo_2O_4 nanoplates, and the insets show the pore size distribution. (a) $FeCo_2O_4$, (b) Co_3O_4, and (c) $NiCo_2O_4$.

Fig. 4. XPS spectra of MCo_2O_4 nanoplates. (a) Fe 2p, (b) Ni 2p, and (c) Co 2p.

Fig. 5. ORR activity of MCo_2O_4 nanoplates. (a-c) LSV curves at rotating speeds from 400 to 2500 rpm, and the insets show the corresponding Koutecky-Levich plots: (a) $FeCo_2O_4$, (b) Co_3O_4, and (c) $NiCo_2O_4$. (d) Comparison of the LSV curves at a scan rate of 5 mV s^{-1} and a rotation rate of 1600 rpm. (e) The corresponding Tafel plots. (f) Current change at a constant potential of 0.2 V (vs. RHE).

Fig. 6. O_2 adsorption pathways on the MCo_2O_4 {111} facets and the corresponding adsorption energies. The relative TOTEN of MCo_2O_4 surface + O_2 molecule in the initial stage is uniformly set to zero.

Fig. 7. PDOS of the adsorbate O* atoms on the MCo_2O_4 nanoplates: (a) Co_3O_4, (b) $NiCo_2O_4$, and (c) $FeCo_2O_4$.

Fig. 8. Discharge polarization and the corresponding power density of Zn-air batteries with MCo_2O_4 nanoplates as the catalyst.

Fig. 9. Cycling stability of Zn-air batteries with MCo_2O_4 nanoplates at 5 mA cm^{-2} (10 min for discharge and 10 min for charge). (a) $FeCo_2O_4$, (b) Co_3O_4, and (c) $NiCo_2O_4$.

500 **Table 1** The relaxed surface areas and surface energies per unit cell of spinel MCo_2O_4 {111}

501 facets.

MCo_2O_4 {111} facets	Cross-section area parameters		Relaxed surface area ($Å^2$)	Surface energy (J)	Surface energy per unit area (J m^{-2})
	a=*b* (Å)	*γ*			
Co_3O_4	5.797	120.0°	29.09	7.88E-19	2.71
$NiCo_2O_4$	5.767	119.1°	29.05	8.52E-19	2.93
$FeCo_2O_4$	5.785	119.3°	29.18	4.68E-19	1.60

502

503 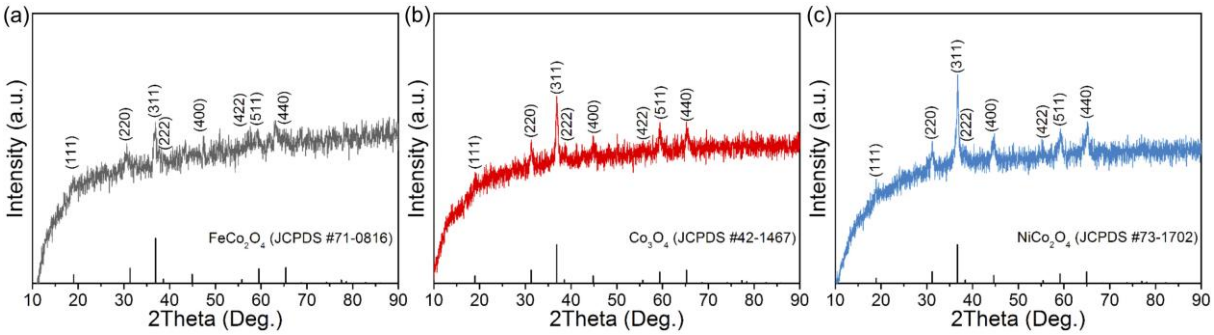

504 **Fig. 1.** XRD patterns of MCo_2O_4 nanoplates. (a) $FeCo_2O_4$, (b) Co_3O_4, and (c) $NiCo_2O_4$.

505

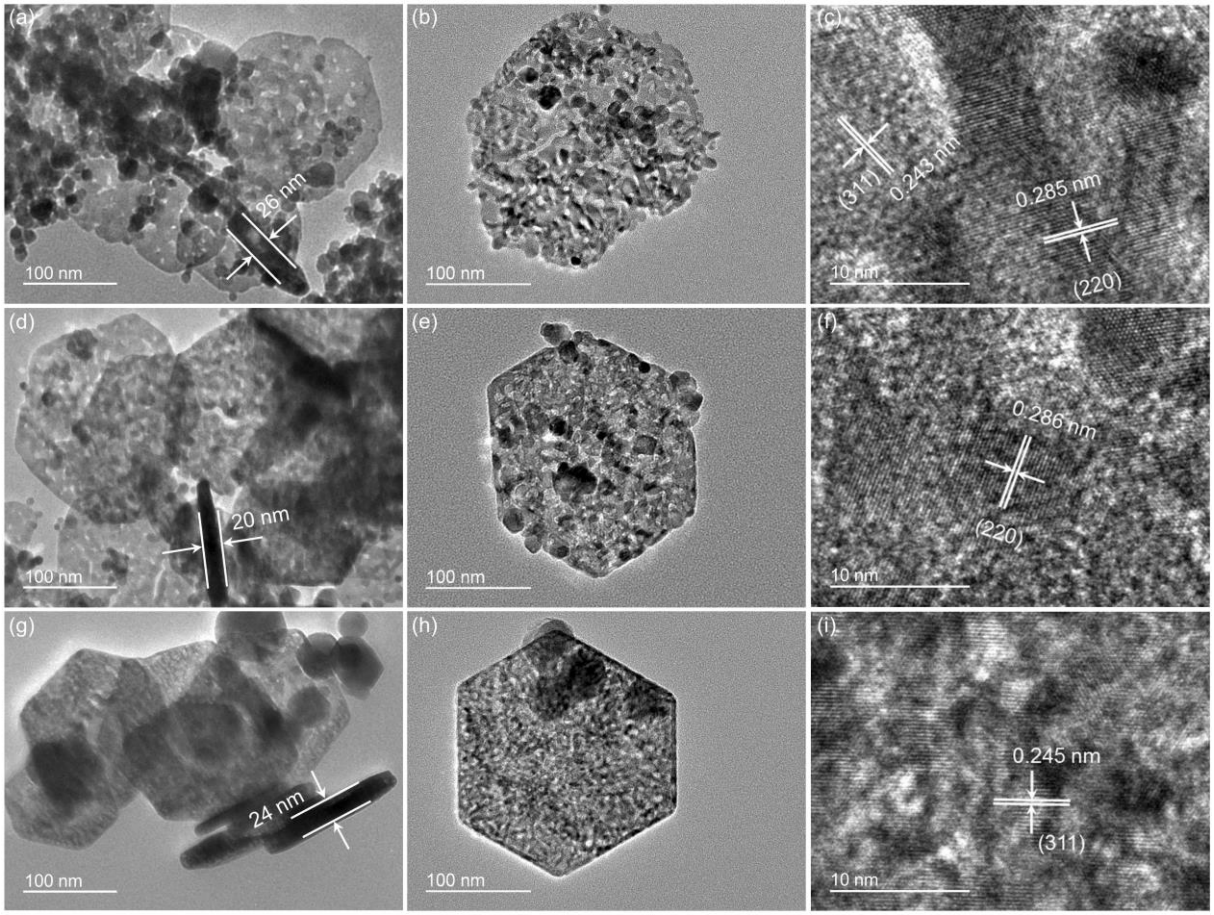

506

507 **Fig. 2.** TEM images of MCo_2O_4 nanoplates with different magnifications. (a-c) $FeCo_2O_4$, (d-

508 f) Co_3O_4, and (g-i) $NiCo_2O_4$.

509

510

511 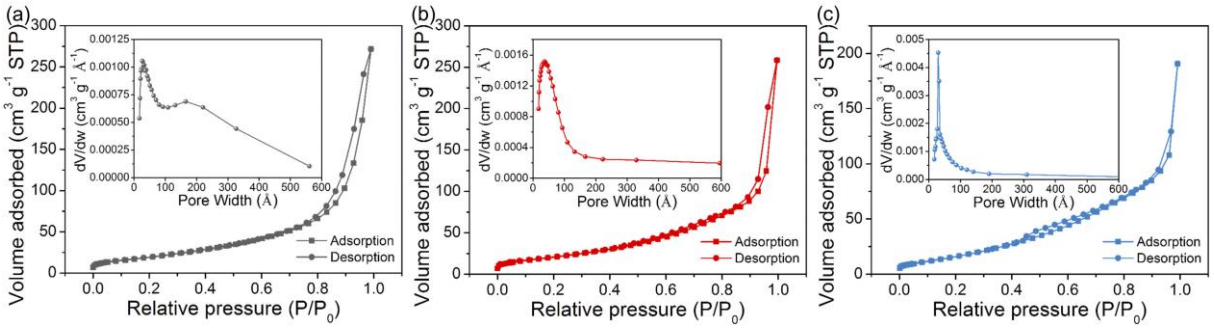

512 **Fig. 3.** Nitrogen adsorption-desorption isotherms of MCo_2O_4 nanoplates, and the insets show

513 the pore size distribution. (a) $FeCo_2O_4$, (b) Co_3O_4, and (c) $NiCo_2O_4$.

514

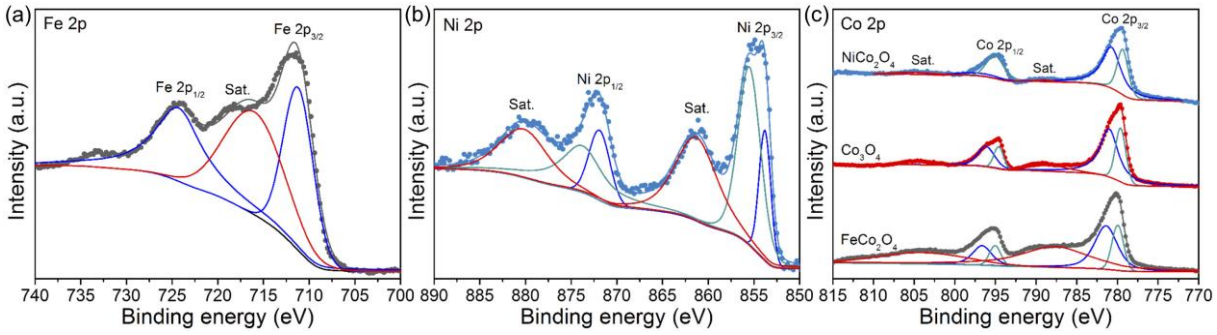

Fig. 4. XPS spectra of MCo_2O_4 nanoplates. (a) Fe 2p, (b) Ni 2p, and (c) Co 2p.

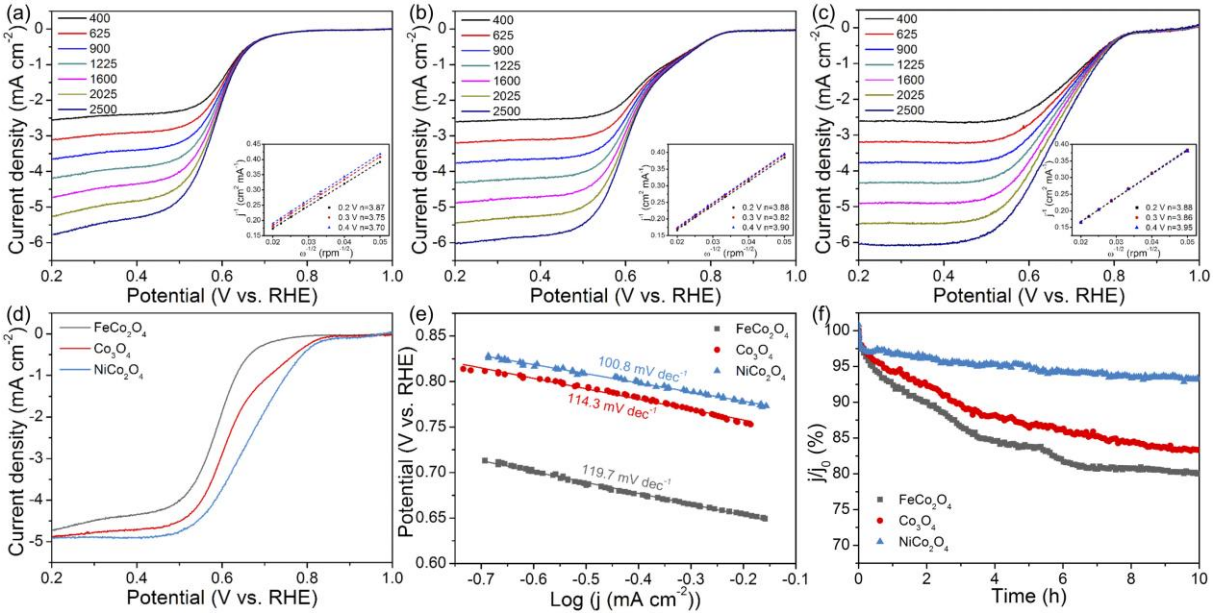

Fig. 5. ORR activity of MCo_2O_4 nanoplates. (a-c) LSV curves at rotating speeds from 400 to 2500 rpm, and the insets show the corresponding Koutecky-Levich plots: (a) $FeCo_2O_4$, (b) Co_3O_4, and (c) $NiCo_2O_4$. (d) Comparison of the LSV curves at a scan rate of 5 mV s^{-1} and a rotation rate of 1600 rpm. (e) The corresponding Tafel plots. (f) Current change at a constant potential of 0.2 V (vs. RHE).

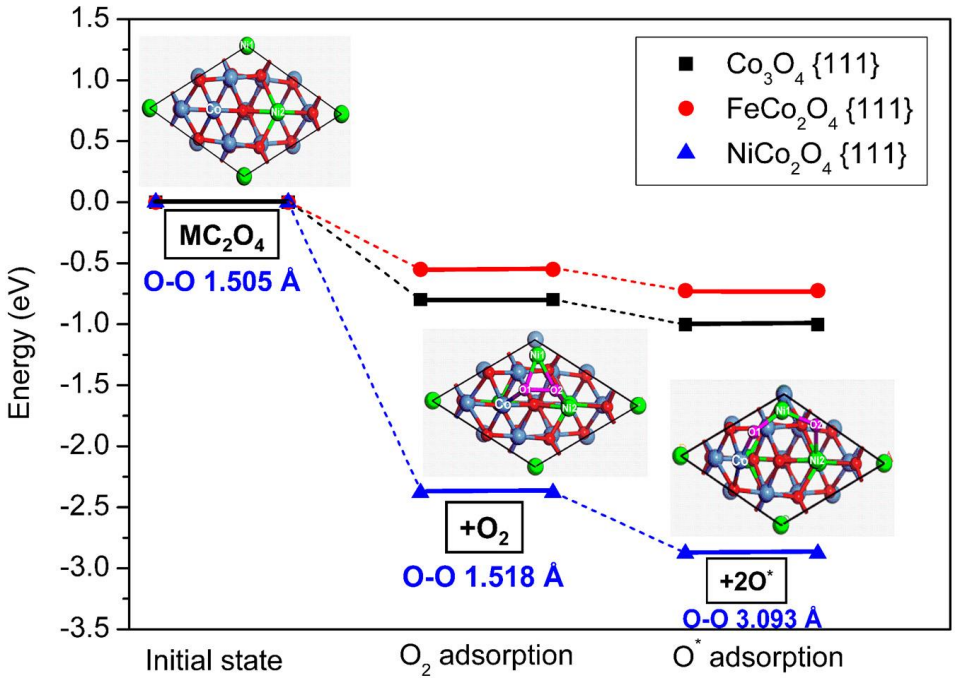

525

526 **Fig. 6.** O_2 adsorption pathways on the MCo_2O_4 {111} facets and the corresponding adsorption
527 energies. The relative TOTEN of MCo_2O_4 surface + O_2 molecule in the initial stage is
528 uniformly set to zero.

529

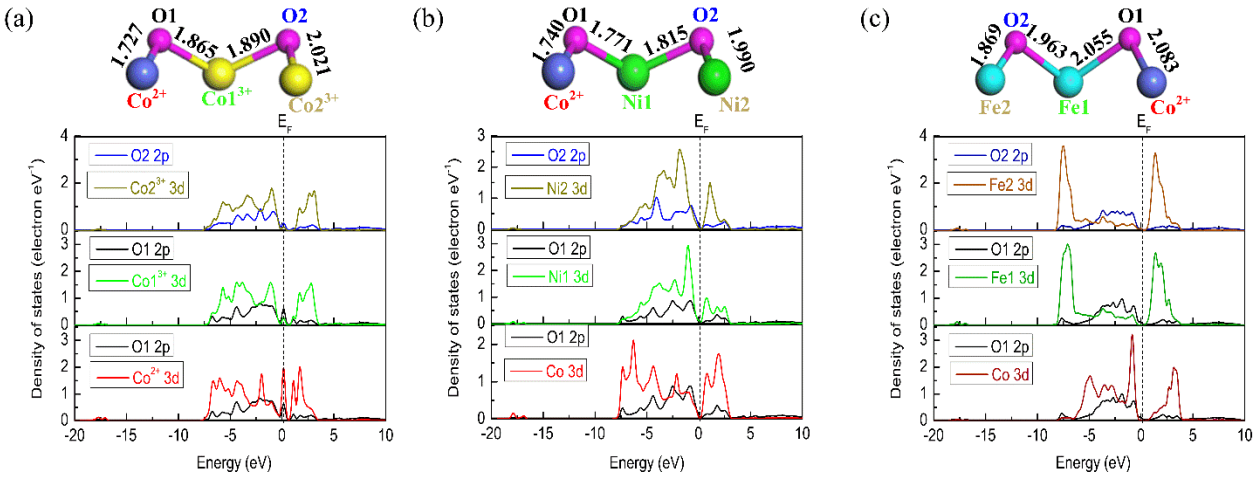

530

531 **Fig. 7.** PDOS of the adsorbate O* atoms on the MCo_2O_4 nanoplates: (a) Co_3O_4, (b) $NiCo_2O_4$,

532 and (c) $FeCo_2O_4$.

533

534

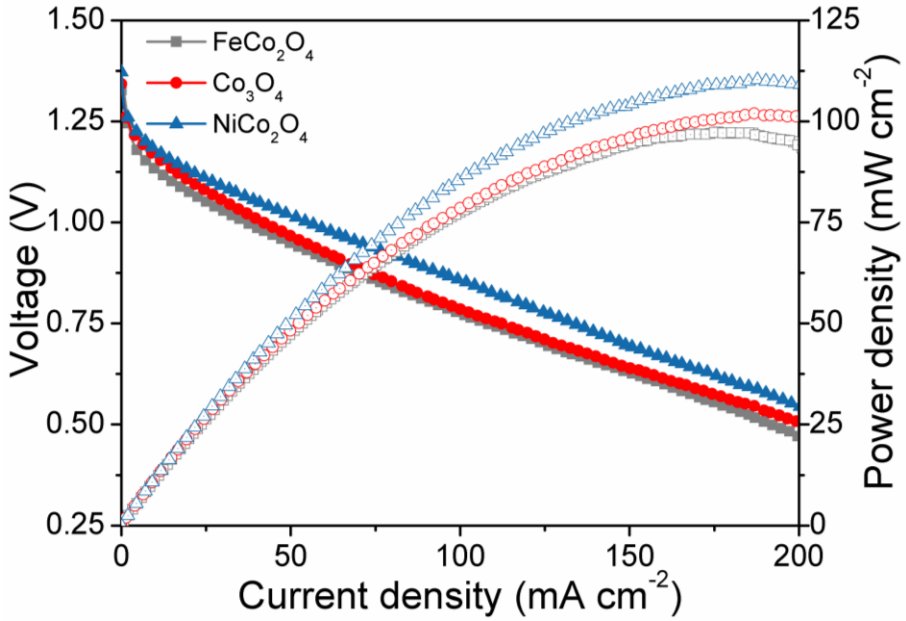

535

536 **Fig. 8.** Discharge polarization and the corresponding power density of Zn-air batteries with

537 MCo_2O_4 nanoplates as the catalyst.

538

539

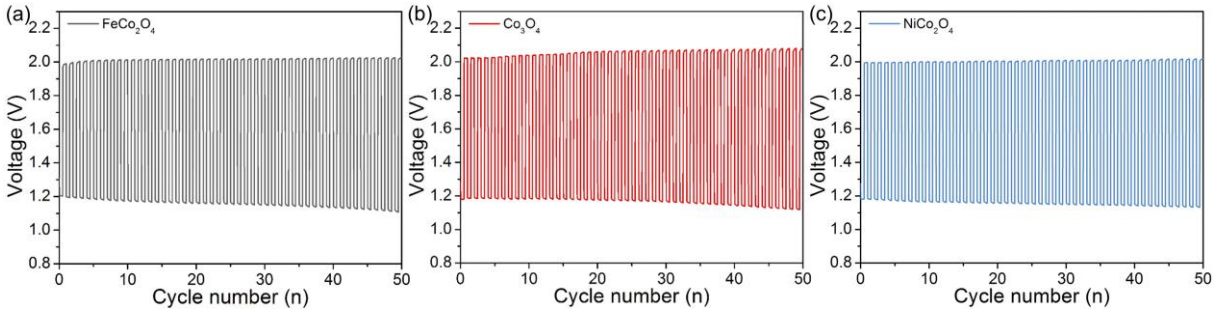

Fig. 9. Cycling stability of Zn-air batteries with MCo_2O_4 nanoplates at 5 mA cm^{-2} (10 min for discharge and 10 min for charge). (a) $FeCo_2O_4$, (b) Co_3O_4, and (c) $NiCo_2O_4$.